Materials Advances

ROYAL SOCIETY OF CHEMISTRY

PAPER

View Article Online
View Journal | View Issue

Cite this: *Mater. Adv.*, 2025, 6, 6094

3D honeycomb porous sulfonated covalent organic polymer (PCOP) synthesized on carbon fabric at refrigerated temperature: supercapacitor and metal-free proton relay for water oxidation in alkaline and neutral media†

Roghayeh Azizi, Mojtaba Shamsipur,* Avat (Arman) Taherpour, Maryam Miri and Afshin Pashabadi*

The sluggish rate of proton transfers during proton-coupled electron transfer is one of the challenges in designing a holistic blueprint for complete biomimicry. Here, we present a one-pot, facile method for the refrigerated synthesis of two different covalent organic polymers by the separate copolymerization of diphenylamine-4-sulfonic acid and diphenylamine with *para*-aminophenol. Substituting diphenylamine with its porous sulfonate analog (PCOP) significantly alters the structural design and proton shuttling characteristics, resulting in remarkable efficiency in the uncommon non-concentrated proton-coupled electron transfer (n-PCET) during OER in both alkaline and neutral media. The functionalized carbon fabric (FCF)/PCOP requires an overpotential of 234 mV at 10 mA cm^{-2}, comparable to metal-based electrocatalysts. A striking semi-reflective boundary condition in the Nyquist plot in acidic media introduces a net capacitive behavior upon protonation of $-SO_3^-$, revealing an ideal capacitor, which has been targeted in the design of a supercapacitor in 0.1 M H_2SO_4 with capacitance C_{sp} = 670.79 F g^{-1}, retaining 89.52% even after 12 000 charge–discharge cycles. Further experimental evidence was obtained by D/H isotope studies, proton inventory, pH dependence analysis, PCOP-water ATR spectroscopy and Gerischer impedance spectroscopy. The results of the DFT studies were used to further explore the structural engineering driven by water clusters and SDS molecules during the cooled synthesis of the COP.

Received 7th May 2025,
Accepted 4th July 2025

DOI: 10.1039/d5ma00451a

rsc.li/materials-advances

1. Introduction

The Grotthuss mechanism, commonly referred to as proton hopping, describes how an excess proton or a proton defect moves through the hydrogen bond network (HBN) in proton-conductive crystalline porous materials.[1] Such self-propelled occurrence proceeds through concomitant creation/cleavage of covalent bonds with adjacent molecules through a low-activation-energy process (E_a < 0.4 eV).[2,3] In the opposite pathway, known as vehicle mechanism, protons are carried through a molecular entity across the plane of a reticular solid proton conductor through low-density proton donor/acceptor media with high activation energy. In earlier mechanisms, dense and orderly arranged proton donors/acceptors permit sufficient degree of reorientation freedom of the protonic species and carriers within 3D un-/shaped channels, which can be helpful for interfacial proton shuttling in heterogeneous catalysis.[3,4] Regulating the level of entanglement and proximity of the exchange sites, as well as the framework's structure, is a principal factor in extending organic frameworks designed for proton transfer (PT) during electrocatalysis and for mimicking the operation of HBN-based proton channels in the active core of photosystem II (PSII) around Mn-cubane in oxygen-evolving catalysts.[5]

This work experimentally tracks the additional functional role tied to the structure-directing agent (SDA, *e.g.*, surfactant), where interfacial perturbation of the water cluster HBN, as the substrate, is characterized *via* attenuated total reflective (ATR) spectroscopy. Covalently-bonded molecular building has been of great interest for the synthesis of adaptable materials with distinct features in recent decades. Emphasizing covalent bonds in fabricating porous covalent structures endows reliable and adaptable chemistry beyond discrete molecules, aiming at

Department of Chemistry, Razi University, Kermanshah, Iran.
E-mail: mshamsipur@yahoo.com, apashabadi@razi.ac.ir

† Electronic supplementary information (ESI) available. See DOI: https://doi.org/10.1039/d5ma00451a

diverse applications. These materials are known as covalent organic polymers (COPs). COPs have amorphous or crystalline nature and are basically characterized by highly cross-linked porous structures that feature robust covalent bonds.[6–8] COPs have been impressively investigated as promising materials for gas storage, proton conduction, and energy applications.[9–20] The abundant pore volume of COPs facilitates mass ion transfer in the electrolyte, allowing impressive processes and fast electrochemical response in energy harnessing and storage devices.[21] However, their capability in PT, specifically multistep proton coupled electron transfer (PCET) reactions in heterogeneous electrocatalysis, has been overlooked compared to competitors such as conductive polymers[4] or the metal-free organic frameworks[3] developed recently by our research groups.

We propose crystalline COP as an advanced-generation, metal-free PCET catalyst, coupled with the unique stability of polymeric structures as we studied in the case of poly-arginine-based guanidine proton relay[4] and our proposed orderly elongated structure of crystalline zwitterionic hydrogen bonded organic framework (ZHOF)[3] in the harsh medium of water oxidation reaction (WOR). Recent advances in the design of covalent organic frameworks (COFs) functionalized with metal nanoparticles have demonstrated enhanced catalytic activity in the oxygen evolution reaction (OER), highlighting the synergistic effects of covalent frameworks and metal sites in electrocatalysis.[22] This approach allows regulating the functionality and investigating the role of diverse functional groups in the crystalline structure, extended through rigidly strong covalent bonds with superior yield of proton hopping *via* water-included organic pores (proton wires).[23] In the O4-water chain within PSII, hydrophobic residues such as D1-Asp61 and Glu354 rigidly fix the water molecules in the H-bond network and serve as hydrogen bond acceptors, which promote the Grotthuss-like mechanism, thereby forming a low-barrier proton wire. Fabricating rigidly arranged reticular COPs fixes proton donors and acceptors in the HBN, reduces the wandering paths of proton motion and minimizes wobbling H-bond directions, thus forming the pre-/post-PT arrays to shuttle protons.

In PSII, the presence of HBN-containing hydrophilic moieties in proton channels intensifies rigidity and strongly latches each group into the other; meanwhile, the hydrophobic motifs in the channel enable water-molecule mobility.[2] OER electrocatalysts often face a PCET imbalance, requiring an interfacial proton acceptor, usually a base solution, which is limited by natural diffusion. This imbalance has led to exploring OER sideways, through proton relays instead of just pure electrocatalysts.

Recent studies emphasize that rational interface engineering through heterostructure formation and strategic doping can significantly modulate interfacial charge distribution and enhance catalytic performance. Such approaches, while often explored in other electrocatalyst contexts, provide valuable conceptual guidance for advancing OER catalysts.[24] In the past decades, the lagged evolution of PT—the sluggish part of PCET—is one of the weaknesses of designing a holistic blueprint for biomimicked artificial leaves. This substantial problem, besides the large proton/electron mass ratio, requires utilizing a solution proton acceptor (OH^-) for the efficient cleavage of O–H bond and liberation of molecular oxygen. Such an intrinsically dictated pathway suffers from the constrained kinetics of the natural diffusion of protonic species (H_2O, OH, H^+) within the diffusion layer and corrosion problems of metal-based electrocatalysts in harsh mediums.[25] The lagging of water delivery and proton shuttling to/from the current collector may also cause incomplete WOR and the formation of reactive oxygen species, $OH^\bullet$, which damage the catalyst frameworks.[23] These limitations are great challenges to achieving full biomimicry, with the ideal being analogous to the active core of the PSII oxygen-evolving complex, which liberates O_2. The advanced deprotonation encourages ''redox leveling,'' which allows for reaching high oxidation states within a limited potential range.

We have successfully developed a straightforward molecular-level design and a controlled method for synthesizing various morphologies, with the apparent distinction of reticularity, for a covalent organic polymer using an oxidative refrigerated synthetic procedure. The overall synthesis involves the combination of diphenylamine-4-sulfonic acid or diphenylamine with *p*-aminophenol. The results elucidate the self-catalytic role of *p*-aminophenol polymer during the oxidative polymerization process. The morphology and functionalities of the product can be directly influenced by reaction parameters such as temperature (refrigeration *vs.* room temperature), the impact of *p*-aminophenol, and the inclusion of surfactants like SDS and the role of water clusters, which has been studied through a detailed DFT study. The existence of a super-hydrophilic SO_3 that can tightly control the rigidity and interfacial reactivity directly drives the OER activity and also energy storage properties of the carbon fabric/PCOP electrode. Eliminating SO_3 from the monomer structure completely changed the reticularity and aborted OER activity at pH $\geq$ 7 and capacitive behavior at pH $\approx$ 1. Various electrochemical studies, such as proteo/deuteron isotopic effects, pH studies, and Gerischer impedance studies, unraveled the detailed mechanistic information of the PCET. An interfacial ATR study was performed to investigate possible agitation of water's HBN, providing mechanistic information. DFT studies were employed to elucidate the formed structures and consider the relative energies of the system.

2. Methods

Fabrication of FCF/COPs

The COPs were synthesized *via* an *in situ* oxidative polymerization strategy under controlled conditions. The functionalized carbon fabric (FCF)@PCOP-SO_3 was prepared using the following steps: briefly, 0.1 M diphenylamine-4-sulfonic acid and 0.1 M *p*-aminophenol were dissolved in 0.1 M H_2SO_4 and stirred vigorously for 30 min, followed by the addition of a 0.1 M SDS solution. After a few minutes of stirring, a 0.1 M $KMnO_4$ solution was added dropwise to the solution under mechanical stirring. In the next step, the treated carbon fiber (CF) pieces were immersed in the mixture at 4 °C for 24 h. FCF@SCOP-SO_3 was synthesized by the same procedure but without SDS.

To demonstrate the crucial role of SO_3 units in the COP for OER, FCF@RCOP electrode was also prepared through chemical polymerization of diphenylamine and *p*-aminophenol under similar conditions in the presence of SDS. Finally, the electrodes were removed from the solution, washed with a mixture of water and ethanol (1 : 1), and dried at 60 °C. To demonstrate the role of temperature, the synthesis was repeated using same procedure in the presence and absence of SDS at room temperature as presented in Fig. S1 (ESI†).

Electrochemical characterization

Electrochemical tests were done with an Autolab instrument (Eco Chemie BV, Netherlands) and using NOVA software (Version 1.10) in a three-electrode cell consisting of Ag/AgCl (3 M KCl) as a reference electrode, Pt wire as a counter electrode, and modified carbon fiber as a working electrode. All electrochemical tests were performed in supporting electrolyte under ambient conditions. We used a potentiostat/galvanostat for linear sweep voltammetry (LSV), cyclic voltammetry (CV), and electrochemical impedance spectroscopy (EIS) measurements, equipped with cell test software for galvanostatic charge–discharge (GCD) studies. The pH of solutions was monitored using a pH meter. The measurements were performed through separately run electrochemical measurements in H_2O and D_2O at several pH(D) values ($pD = pH_{read} + 0.41$).[3,4] The pH(D) in both water and deuterium solutions was adjusted to by KOH and K_3PO_4, respectively. K_3PO_4 was utilized in this study because the investigation into proton transfer showed that there was no dependence of OER activity on K_3PO_4, as will be elaborated on below.

3. Results and discussion

To functionalize the CF with COPs, a versatile synthetic route is shown in Scheme 1(A). Three types of FCF@COPs were synthesized *via* chemical polymerization using *p*-aminophenol and substituted diphenylamine derivatives (diphenylamine or diphenylamine-4-sulfonic acid) in the presence of $KMnO_4$ as an oxidant and sulfuric acid as a solvent. In the first path, *p*-aminophenol, as a linear building block, was combined with an electron-donating diphenylamine moiety in the presence of SDS, by a one-pot procedure under acid and oxidant, which gave reticular COP on CF substrate (FCF@RCOP). The formed RCOPs can join FCF filaments through hydrogen bonds, electrostatic interactions, and π–π electron donor–acceptor interactions. In the second path, instead of diphenylamine, the same amount of diphenylamine-4-sulfonic acid was employed to give porous sulfonated COP on the FCF electrode support (FCF@PCOP-SO_3). The proposed profile of the polymer structure, including APA-SO_3 + pAP, is shown in Scheme 1(B). In the third path, a similar procedure as applied for FCF@PCOP, but in the absence of SDS, resulted in the formation of spherical sulfonated COP (FCF@SCOP-SO_3), as revealed by FE-SEM. Also, previously, the influence of SDS concentration on the molecular architecture of polymers has been proven.[26] Subsequently, the OER performance of the resulting three types of COP electrode filaments, FCF@RCOP, FCF@SCOP-SO_3, and FCF@PCOP-SO_3, was evaluated.

The morphology of the various synthesized samples was examined using FE-SEM. As illustrated, the morphologies of FCF@RCOP, FCF@SCOP-SO_3, and FCF@PCOP-SO_3 differ from one another. Fig. 1(A) depicts RCOP, which exhibits a stacked polymer morphology. For SCOP, the polymerization of diphenylamine-4-sulfonic acid and *p*-aminophenol in an aqueous solution resulted in a distinctive spherical structure of varying sizes (Fig. 1(B)), attributed to the formation of the COP influenced by water clusters (as detailed in the computational section). This observation is further supported by the notably difficult drying of the residues in the beaker in the case of SCOP. Fig. 1(C) illustrates that the FCF is entirely enveloped by PCOP-SO_3. The magnified view reveals that the PCOP-SO_3 components interconnect to create a porous structure with a honeycomb-like appearance. Additionally, the presence of SDS inhibits the formation of water-cluster-driven SCOPs, significantly influencing the structure's morphology.[27]

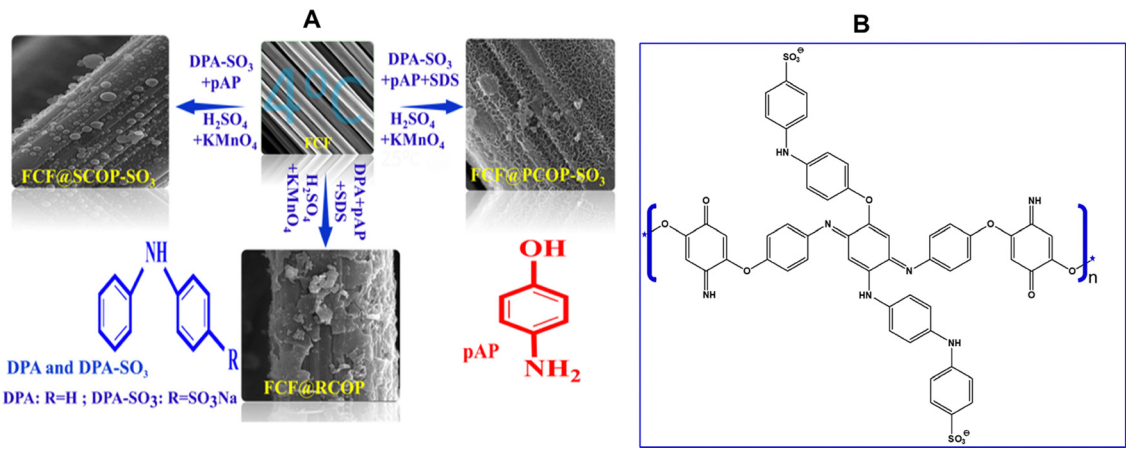

Scheme 1 (A) Synthesis and schematic illustration of FCF@RCOP, FCF@SCOP-SO_3, and FCF@PCOP-SO_3 from *p*-aminophenol, and substituted diphenylamine at 4 °C. (B) The proposed profile of the synthesized polymer including DPA-SO_3 + pAP.

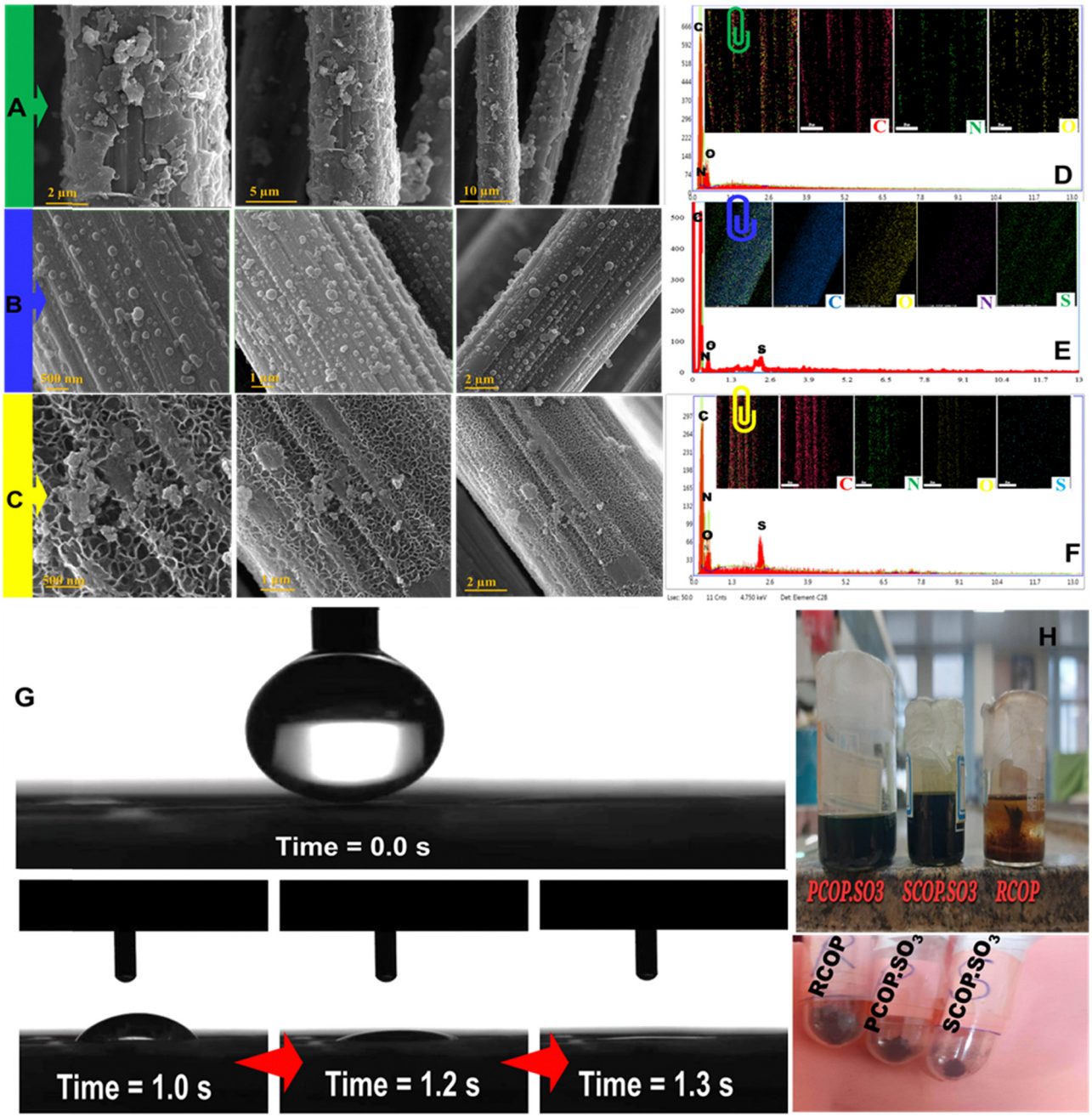

Fig. 1 FE-SEM images and the corresponding elemental mapping images of the (A) FCF@RCOP, (B) FCF@SCOP-SO_3 and (C) FCF@PCOP-SO_3. (D)–(F) are the equivalents EDXA and mapping analyses from (A) to (C) respectively. (G) The time-lapse of the contact angle experiment undertaken on FCF@PCOP-SO_3. (H) the The dried synthesized COPs collected from the bottom of the beaker and the corresponding solution prior to filtration and drying.

The mapping analyses indicate that SCOP-SO_3 (Fig. 1(E)) and PCOP-SO_3 (Fig. 1(F)) contain oxygen, nitrogen, sulfur, and carbon. The presence of sulfur in the polymer, as confirmed by the results, validates the successful synthesis. In contrast, RCOP is composed solely of nitrogen, oxygen, and carbon elements (Fig. 1(D)). The hydrophilicity of the synthesized COP was assessed through contact angle measurements. The relevant image can be found in Fig. 1(G), along with the Supporting Videos VS1 and VS2 (ESI†). Fig. S2 (ESI†) displays the bare FCF at different magnifications, showing no changes in the morphology of the carbon fiber.

Computational modeling

Modeling of IR and ^{1}H-NMR spectra of the discussed polymer structures was performed using QM methods (DFT-B3LYP/6-31G*). In view of the large structures, the results of modeling for water clusters, folding and unfolding of the discussed modeled polymer processes with water clusters, SDS effects

and the related energies in the stages have been obtained by MMFFaq method. The calculations were carried out with the Spartan '10 package. As described in morphological studies, during the synthesis, we triggered the oxidative condensation reaction of diphenylamine-4-sulfonic acid and *p*-aminophenol in the presence of $KMnO_4$ under refrigeration. The graphite-supported COP was subjected to SEM studies, and results disclosed a uniform spherical morphology without any porosity. This synthetic pathway was repeated once with the addition SDS (>CMC critical level), and the synthesized COPs displayed an orderly arranged honeycomb, resembling a porous structure.

Herein, to investigate the function of water clusters during synthesis in aqueous environments, a model was created using 150 water molecules that are interconnected through hydrogen bonds. In Fig. 2, from left to right, we tracked the steps of scavenging of the water cluster ($n$$H_2O$) by the modeled polymer. In Step 1, the modeled polymer has started folding around the water cluster through H-bond *via* functional groups (–OH, $–NH^-$, $–NH_2$, $–SO_3^-$), eventually curving around and completely capturing the water cluster (step 2). These two stages are depicted by a hand-ball illustration. Outside the dashed rectangle, we consider the polymer further unfolding from around the cluster upon SDS treatment. The modeled SDS (shown as a spoon) withdraws the H_2O molecules from the main water cluster ($n$$H_2O$) by its H-bond accepting agents ($–SO_3^-$ functional group at the end of aliphatic chain). In the next steps (steps 2 and 3), the polymer has completed unfolding around the water cluster ($n$$H_2O$), and some of the SDS molecules separated H_2O molecules from the main water cluster and some other parts made a great micelle. In step 4, the modeled polymer has completely opened and unfolded, releasing the water cluster. The micelles formed between the SDS + water cluster can direct the growth of the uncapped (opened) polymer. These micelles have an interfacial hydrophobicity that can impede the spherical growth and establish a porous structure.

Fig. 3(A) and (B) show the differences in free energies (in kcal mol^{-1}) between the unfolded model polymer and the water cluster with the model polymer folded around the water cluster by the discussed H-bonding agents. The energy gap was calculated to be 60.6 kcal mol^{-1}. In the presence of SDS, the differences in free energies were calculated to be about 14.7 kcal mol^{-1} in this modeling. In the next step, to reach the unfolded modeled polymer and the water cluster ($n$$H_2O$), the difference of free energy is 45.9 kcal mol^{-1}. It is worth expressing that the formation of the mega complex (polymer + water cluster), as an exothermic reaction, releases energy. This phenomenon is consistent with the occurrence of the exothermic reaction under refrigeration, as explained in the experimental section.

Fig. S13 (ESI†) shows the modeled structure for the discussed polymer and the calculated IR spectrum of the discussed modeled polymer by B3LYP/6-31G* method. The vibrations of the functional groups are shown (3500–4000 cm^{-1} for H-bonding agents –OH, –NH–, $–NH_2$, $–SO_3^-$). The additional details of the vibrational frequencies for the functional groups are shown in the calculated IR spectrum (1250–1450 cm^{-1} for $–SO_3H$ functional group).

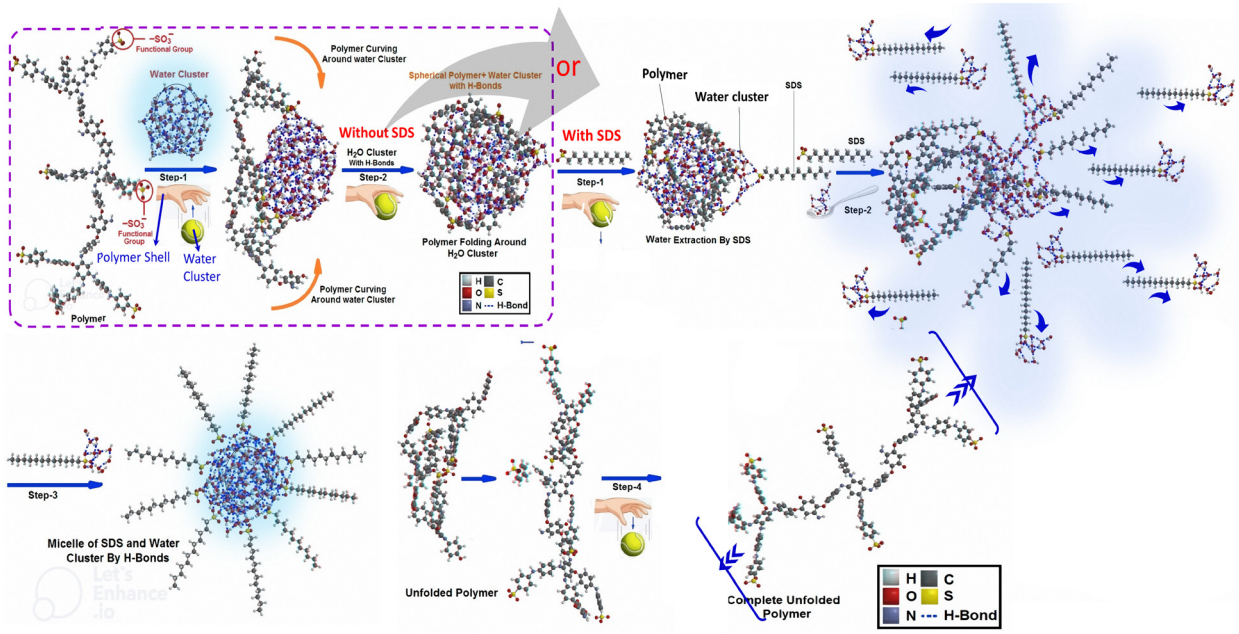

Fig. 2 The steps of the water cluster ($n$$H_2O$) scavenging shown by the polymer model. Without SDS, in Step 1, the polymer initiates folding around the water cluster throughs H-bonding residues (–OH, $–NH^-$, $–NH_2$, $–SO_3^-$), completely folding in step 2. (These two stages are depicted by the hand and ball.) In the presence of SDS, in the first step, the modeled SDS (like a spoon) has started withdrawing the H_2O molecules from the main water cluster by the $–SO_3^-$ functional group at the end of the aliphatic chain. In the next steps (steps 2 and 3), the polymer has completed unfolding around the water cluster, and some of the SDS molecules separated H_2O molecules from the main water cluster and some other parts made a great micelle. In step 4, the modeled polymer has completely opened and unfolded, releasing the water cluster.

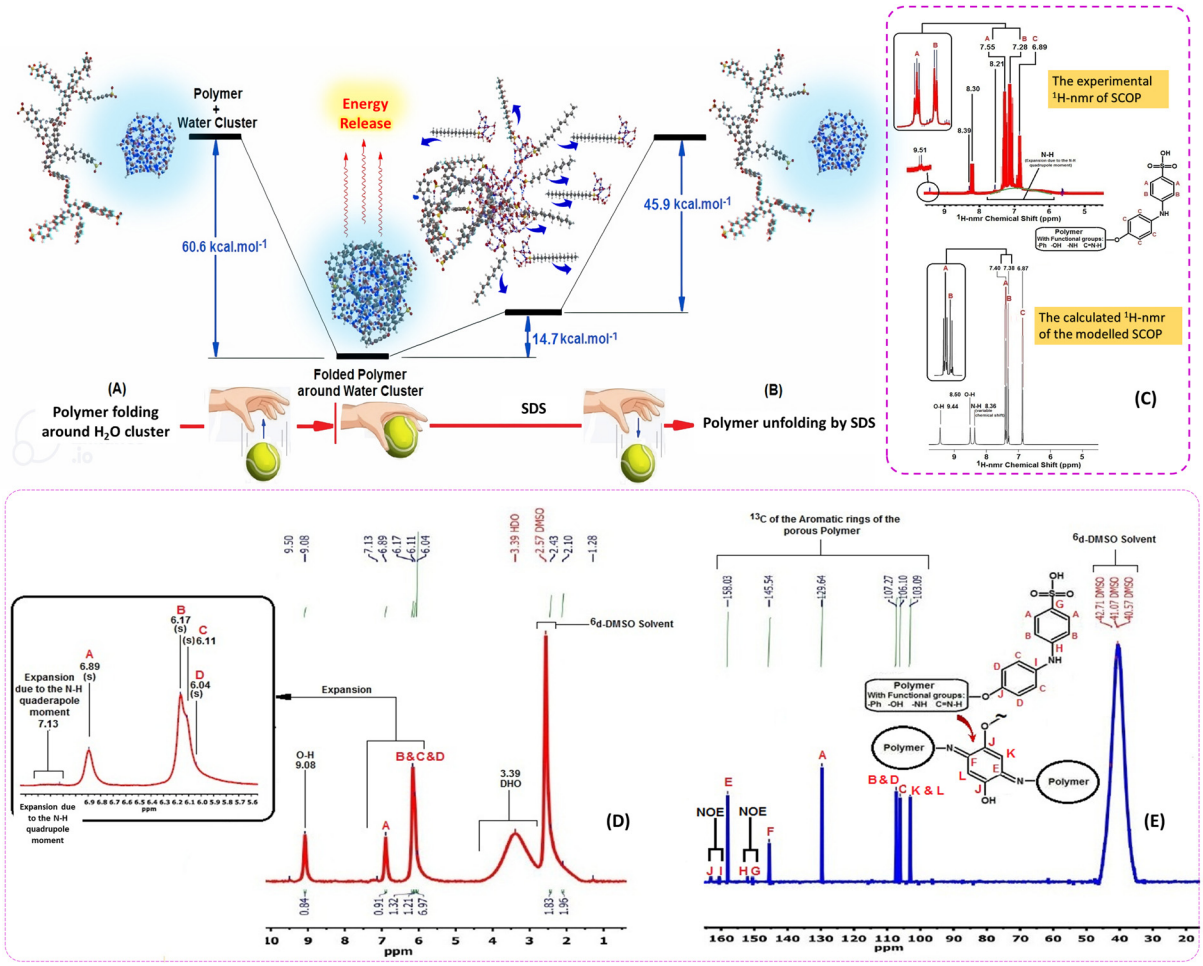

Fig. 3 (A) The differences in free energies (in kcal mol^{-1}) between the unfolded modeled polymer and the water cluster with the modeled polymer folded around the water cluster by the discussed H-bonding agents (the energy gap was calculated to be 60.6 kcal mol^{-1} in this modeling). (B) The modeled SDS triggers the withdrawal of H_2O molecules from the water cluster (ΔG = 14.7 kcal mol^{-1}). In the next step, to reach the unfolded modeled polymer and the water cluster, the difference in free energy is 45.9 kcal mol^{-1}. (C) The experimental ^{1}H-NMR spectrum of the discussed polymer (top) and the calculated ^{1}H-NMR spectrum of the discussed polymer (bottom) using the B3LYP/6-31G* method. There is good agreement between the experimental and theoretical results of the ^{1}H-NMR spectra. (D) The experimental ^{1}H-NMR spectrum of the porous form of the discussed polymer. (E) The ^{13}C-NMR spectrum of the porous form of the discussed polymer.

The stretching O–H groups in the discussed structure are shown on the right side of the IR spectrum. The signals between 2700–3700 cm^{-1} of the experimental ATR results could be compared with the calculated IR spectrum. In Fig. 3(C), the ^{1}H-NMR spectrum of the modeled SCOP calculated by the B3LYP/6-31G* method shows good agreement with the results of the experimental ^{1}H-NMR spectrum. The signals between 6.89 and 7.55 ppm in the experimental and between 6.87 and 7.40 ppm in the calculated spectrum concern the H-aromatics. The broad signal between 5.90 and 7.90 ppm concerns the N–H; its extension probably is related to the N–H quadrupole moment of the N atom. The doublet and triplet (at 7.28 and 7.55 ppm, respectively) agree well with the calculated ^{1}H-NMR spectrum at 7.38 and 7.40 ppm for the HA and HB of the aromatic rings. The signals of the experimental ^{1}H-NMR spectrum between 8.30 and 9.51 ppm are related to the H-bonding agents (–OH, –NH–, –NH_2, –SO_3^- functional groups located on the aromatic rings), which match the theoretical ^{1}H-NMR spectrum (8.36–9.44 ppm). Fig. 3(D) and (E) show the experimental ^{1}H-NMR and ^{13}C-NMR spectra of PCOP, with good agreement between the experimental and theoretical spectra. The signals of DMSO and DHO (solvent signals) appeared at 2.43 and 3.39 ppm, respectively. The signals between 6.04 and 7.13 ppm concern the H-aromatics in the porous form of the discussed polymer. These signals were shifted to 6.89–7.55 ppm in the spherical form (SCOP). In Fig. 3(D), the broad signal between 7.00 and 7.35 ppm relates to the N–H; its expansion probably relates to the N–H quadrupole moment of the N atom, which shows a broad shifted signal between 5.90 and 7.90 ppm. The doublet and triplet (at 7.28 and 7.55 ppm, respectively; as A, B and C signals) in SCOP agree well with the calculated ^{1}H-NMR spectrum at 7.38 and 7.40 ppm for the HA and HB of the aromatic rings.

The signals (Fig. 3(C)-experimental ^{1}H-NMR spectrum) between 8.30 and 9.51 ppm concern the H-bond-making agents

(–OH, –NH–, $–NH_2$, $–SO_3^-$ functional groups located on the aromatic rings), which match with the theoretical Fig. 3(D) results of ^{1}H-NMR spectrum (8.36–9.44 ppm). This type of signal in the ^{1}H-NMR spectrum disappeared in the porous form of the discussed polymer. Fig. 3(E) shows the H-spin decoupled from the ^{13}C-NMR spectrum of the porous form of the discussed polymer. The strong and broad signal of DMSO (solvent signals) appeared at 40.6 and 42.7 ppm. The signal at 129.6 ppm is related to CA atoms of the aromatic ring in the porous form of the discussed polymer. The signals of CB and CD atoms of the aromatic ring in the porous form of the discussed polymer appeared at 107.3 ppm. The signals of CC atoms of the aromatic ring in PCOP appeared at 105.1 ppm, and the signals of CE and CF atoms of the other part of the aromatic ring in appeared at 145.5 and 158.0 ppm, respectively. The signals of CK and CL atoms of the cyclohexa-2,5-diene-1,4-diimine moiety appeared at 103.1 ppm. Moreover, the weak signals between 150–155 ppm and 160–165 ppm concern the 4 °C atoms (G, H, I and J) of the aromatic and cyclohexa-2,5-diene-1,4-diimine parts of the discussed polymer. These 4 °C atoms are under the nuclear Overhauser effect, so they appeared as weak signals. The results show good agreement with the calculated data.

Electrochemical studies

The as-prepared electrodes were used as the working electrode in a typical three-electrode system to examine their OER activity in alkaline and neutral media as metal-free PCET catalysts (Fig. 4). All electrodes were synthesized using FCF as a flexible metal-free current collector with extreme stability in the harsh medium without any corrosive tendency. The LSVs were obtained in 0.1 M of KOH with a sweep rate of 5 mV s^{-1} without further IR correction. The voltammograms in alkaline medium demonstrate no early-stage activity in CF and characterized the CF as a non-metallic substrate where no significant activity observed. Given the different strategy of refrigerated synthesis, the main parameters are due to the role of sulfonate residues and also the influence of the structural directing agent (SDS molecules). The fabricated electrodes, FCF@RCOP (Fig. 4(A), curve c), FCF@SCOP-SO_3 (curve d) and FCF@PCOP-SO_3 (curve e), were compared for OER activity, and the equivalent results show a dramatic catalytic activity at FCF@PCOP-SO_3 compared to FCF@RCOP-SO_3 and FCF@SCOP-SO_3. The current density at 1.9 V *vs.* RHE was found to be increased from 28 to 339 mA cm^{-2} (more than 12-fold enhancement) in 0.1 M of KOH. The onset of the catalytic WOR shifted from 1.821 at FCF to 1.498 at FCF@PCOP-SO_3, a pronounced negative shift as much as 323 mV (see Fig. S11, ESI†). To further explore the electrocatalytic activity of the synthesized COP, the same electrochemical measurement was conducted in neutral medium (PBS 0.1 M pH = 7), and the relevant LSVs exhibited an apparent negative shift from 1.733 at FCF to 1.405 at FCF@PCOP-SO_3 with the overpotential of J = 5 mA cm^{-2} (η@5 mA cm^{-2}), indicating advanced PCET reaction taking place at the interface of the sulfonated porous electrode (Fig. 4(B)). The calculated Tafel slopes in pseudo-polarized conditions revealed a dramatic decrease from 467 to 165 mV dec^{-1} for CF toward FCF@PCOP-SO_3.

To compare the relative signal stability after two weeks, the measurements were repeated under the same conditions, and the corresponding voltammograms are presented in Fig. S14 (ESI†). Also exhibited is excellent long-term electrochemical stability under OER conditions (Fig. S12, ESI†).

pH dependency

We consider in following whether the operation of the sulfonated metal-free PCET catalyst is associated with the mechanism of non-concerted PET processes, giving rise to pH-dependent OER activity. Calculating the pH dependency of the OER kinetics on the RHE scale can provide a deep insight into the reaction pathway, especially the degree of de-/coupling of PT/ET during the overall reaction. Herein, we studied the

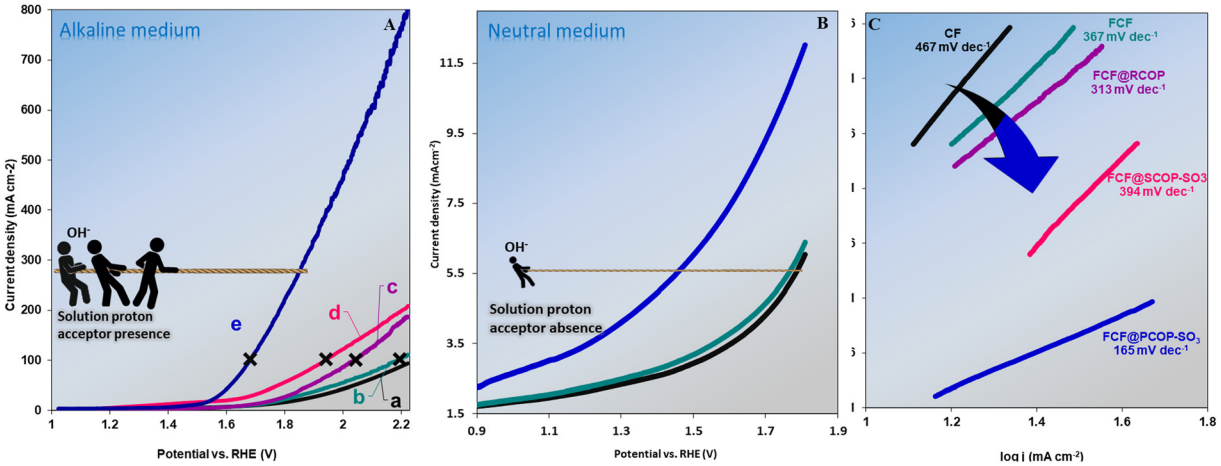

Fig. 4 (A) and (B) LSVs recorded in 0.1 M of KOH and phosphate buffer (pH=7), respectively, with a sweep rate of 5 mVs^{-1} at (a) CF, (b) FCF, (c) FCF@RCOP, (d) FCF@SCOP-SO_3 and (e) FCF@PCOP-SO_3. (C) The corresponding Tafel plot for CF (blue), FCF (brown), FCF@RCOP (green), FCF@SCOP-SO_3 (violet) and FCF@PCOP-SO_3 (red).

degree of concertedness or non-concertedness and the reaction order of the catalytic processes over FCF@PCOP-SO_3. RHE was used as the reference electrode to ensure that the overpotential *versus* equilibrium potential of O_2/H_2O remained consistent at various pH levels. The variation in OER activity on the RHE scale *vs.* pH suggests a non-concerted PET, where the RDS is either a PT or preceded by acid/base equilibrium.[28] The conventional metallic-based OER electrocatalysts show pH-independent behavior, which implies a concerted-type PCET approach.[3,28,29] The LSVs (Fig. 5(A)) obtained for the FCF at different pH values show a pH-independent behavior, indicating a conventional concerted mechanism of PCET. In contrast, the OER activity on the RHE scale for FCF@PCOP-SO_3 becomes higher with increasing pH, indicating a non-concerted PET coupled to the proton-shuffling bonded surface species responsible for the yield of the overall OER. The reaction order of OER activity with pH demonstrates how the OER kinetics depends on the proton activity. A primary-order chemical reaction implies linear dependence on H^+ activity, *i.e.*, linear dependence on pH, while a zeroth-order chemical reaction would indicate no dependence.[30] As illustrated in Fig. 5(B), the reaction orders, determined from the slope of the log*J versus* pH plot (within the potential range of 1.52 to 1.64 V), ranges from 0.129 to 0.148. This fractional non-zero reaction order imparts an n-CPET mechanism, where protons are involved in several complex chains and side reactions. Furthermore, the degree of non-concertedness indicates the intermediates are stabilized by a strong H-bond network, which are separate from the initial and final equilibrium configurations.

Isotopic studies

Deuterium/proton kinetic isotope effect (KIE) studies were conducted to estimate the efficiency of PT as part of the PCET process and the dependence of the rate-determining step (RDS) of OER on ET/PT. Theoretically, the KIE is calculated from the ratio of rate constants (K_{H_2O}/K_{D_2O}), which are respectively proportional to *J*-H_2O and *J*-D_2O. A primary KIE (PKIE), that is, a KIE value larger than 1.5, indicates that the PT occurs at the RDS or at least in one of the steps affecting the kinetics of PCET. KIE values <1.5 (designated as secondary KIE, SKIE) suggest no noticeable PT is involved in the RDS:[3]

$$\mathrm{KSIE} = \frac{J_H(K_H)}{J_D(K_D)} \quad (1)$$

Electrochemical measurements were carried out by obtaining LSV plots in H_2O and D_2O media at the same pH(D), where the pD value was calculated from the equation pD = pH_{read} + 0.41. KOH and K_3PO_4 basic solutions were utilized to adjust pH or pD. The resulting LSVs expressed the same isotopic behaviors for CF (Fig. 6(A)) and FCF (Fig. 6(B)) during the WOR. Over all potentials, both electrodes showed lower current density in the deuteron solution compared to those in the proton solution. The KIE values over the potential range of 1.7 to 1.9 V *vs.* RHE ranged from *ca.* 1.8 to 2.4, these primary KIE values (>1.5) indicate an O–H bond cleavage in the RDS.[3,4,31] A slight decrease observed at the FCF, ranging from 3% to 15% (at different potentials), may be related to the participation of interfacial functions on the FCF, indicating

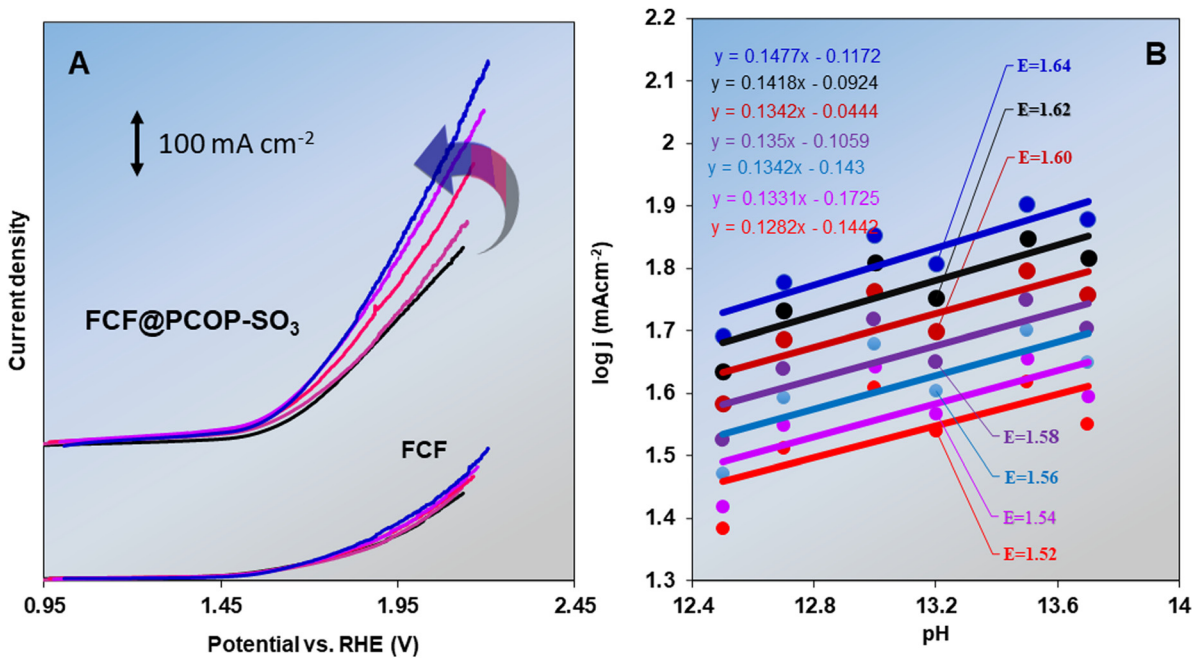

Fig. 5 (A) LSVs over the pH range of 12.5 to 13.7 for both FCF and FCF@PCOP-SO_3; (B) the plot of log*J vs.* pH exhibits fractional reaction orders of 0.12–0.14 at different potentials.

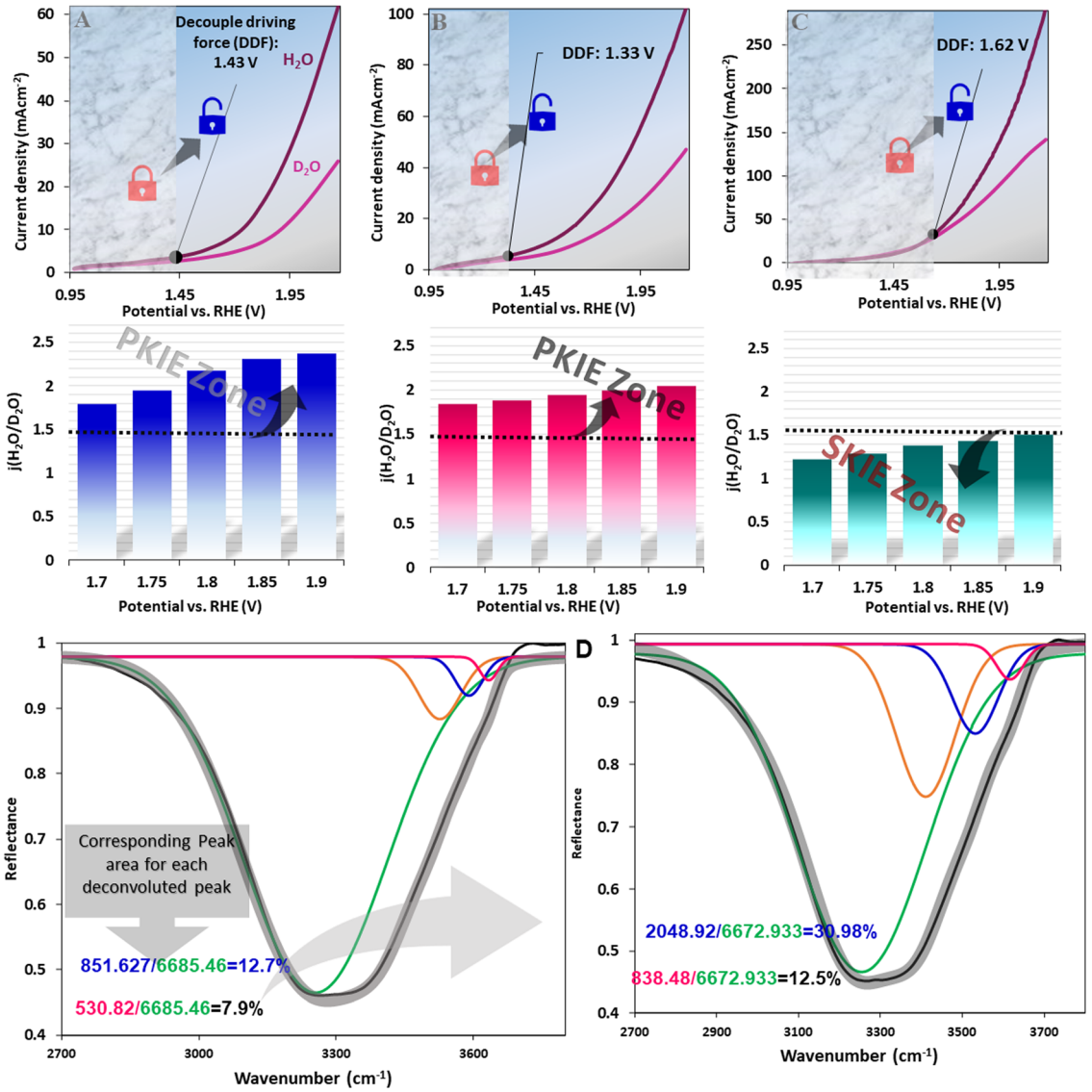

Fig. 6 Kinetic isotopic effect studies, with LSVs recorded in H_2O (violet) and D_2O (red) at (A) the CF with KIE@1.85 V of 2.30, while (B) the FCF discloses a KIE@1.80 V of 1.94 at (C) FCF@PCOP-SO_3 with KIE@1.75 V of 1.28, as low as 1.5 by the acceleration of ET. The bottom row represents the equivalent plots of KIE changes against the anodic potentials. (D) The OH-stretching IR band (thick) and its Gaussian components (thin) for CF + water (left) and FCF@PCOP-SO_3 + water (right). The plots show the experimental line shape (transparent black), curve fit (black), and four resolved components in blue, purple, pink and green, corresponding to OH stretching of H-bonded water aggregates with cluster numbers of 3, 2, 1 and non-H-bonded bonded water, respectively.

that the CF may perturb the PCET process during low-yield WOR undertaken at the FCF.

The lagging of JD at higher driving forces may be related to the acceleration of ET, revealing a difference in the bond breaking of O–D/O–H, due to the shorter bond length of O–D being energetically unfavorable in PCET compared to the O–H bond. Therefore, in an energy threshold, this difference is revealed, resulting in a KIE >1. Fig. 6(C) shows the equivalent LSV at FCF@PCOP-SO_3 with a dramatic decrease of KIE, ranging from 1.23 to 1.49 over the potential window of 1.7 to 1.9 V. Increasingly positive potentials cause the observable differences, although still, the KIE falls into the SKIE region with no PT in RDS, which can be related to the relatively delayed PT upon acceleration of ET. However, despite the increase in ET rate at higher overpotential, O–H bond cleavage does not occur in the RDS, implying the high capability of FCF@PCOP-SO_3 in proton transport. Comparing the LSVs at FCF@PCOP-SO_3 with the two former cases reveals an increased decoupling driving force (DDF) of 1.62 V, signifying that the proposed proton relay facilitates an effective PT during the PCET processes. The shift of the DDF from 1.43 for CF to 1.62 for FCF@PCOP-SO_3 indicates a coupling of ET/PT over a greater sweep potential, where the higher kinetics of ET does not lead to delay of PT when protons are substituted with deuterium.

We investigated the role of the robust interfacial sulfonates as *in situ* heterogeneous stimuli on water's HB network, where the successful adsorption events of protonic species can be controlled. Using attenuated total reflection infrared spectroscopy

(ATR-IR), we compared the broad OH-stretching band of water, 2800–3700 cm^{-1}, to explore the extensive HB agitation by COP, a critical event that may directly predominate the vibrational modes and the different degrees of the freedom for the water molecules beyond the adsorption of substrate, as the first step of the heterogeneous WOR. After recording the ATR spectra for CF + water and FCF@PCOP-SO_3 + water, the OH-stretching bands were deconvoluted to the four sub-bands of water, denoting the multiple degrees of HB modes.[32,33] Fig. 6(D) shows the results of the curve-fitting analysis of the FTIR spectra for CF + water and FCF@PCOP-SO_3 + water, singly. The resolved spectra displayed four peaks, from *ca.* 3200 cm^{-1} to 3600 cm^{-1}, corresponding to triply, doubly, and singly hydrogen-bonded and free (non-hydrogen bonded) H_2O, respectively.[34,35] The degree of breaking of the HB network (DBHB), as the ratio of calculated peak area of the free (pink) and singly (blue) bond water spectra around 3600 cm^{-1} to that of the hydrogen-bonded water molecules around 3200 cm^{-1} (green curve), were respectively found to be 7.9–12.7% and 12.5–30.98%, respectively, for CF + water and FCF@PCOP-SO_3 + water. The increased DBHB for FCF@PCOP-SO_3 compared to CF + water elucidates the increased delivery of free water molecules and efficient capability of sulfonate residues in the perturbation of the water HBN, which directly improves the success of adsorption events during heterogeneous WOR.[34]

Energy storage studies

Considering the observation of a semi-reflective boundary condition in the Nyquist plot of the PCOP in H_2SO_4 (see Fig. 8), indicating a net capacitive behavior, a detailed electrochemical study was conducted to unravel the capacitive characteristics of the FCF/PCOP and graphite paper/PCOP. The highly functional honeycomb COP offers an ideal framework for the diffusion and retention of ions, making it an appealing option for the development of charge storage devices. The CV was conducted in a three-electrode system to assess the stable electrochemical window prior to assembling the supercapacitor (SC). Fig. 7(A) displays the CV curves for the FCF@PCOP-SO_3, FCF, and CF electrodes recorded over a potential range (ΔV) of *ca.* −0.9 to 0.01 V in 0.1 M H_2SO_4 aqueous electrolyte. The capacitive performance of FCF@PCOP-SO_3 was significantly increased compared with both FCF and CF. FCF@PCOP-SO_3 presents a characteristic rectangular-like curve with a nearly ideal capacitive behavior.

Long-term cyclic stability is another vital factor that should be considered to estimate the capacitance constant alterations (Fig. 7(B)). The curve of the CV data for the FCF@PCOP-SO_3 is maintained until around 1000 cycles without a change in the loop area, with excellent reversibility within the operating potential window. As illustrated in Fig. 7(C), it shows remarkable long-term CV stability, maintaining over 97.56% specific capacitance performance (C_{sp}) even after 2000 cycles. The C_{sp} of the FCF@PCOP-SO_3 can be estimated from the CV curves using the following equation:[36]

$$C_{sp} = \left(\frac{\int I(V)\mathrm{d}V}{\Delta V m \nu}\right), \quad (2)$$

where V (V) and I (A) are the potential and current; ΔV (V) is the potential window; ν (V s^{-1}) is scan rate and m (mg) is the material mass of the COP synthesized on the surface of FCF. As illustrated in Fig. 7(D), the curve remains semi-rectangular as the potential window is gradually increased from 0.17 to 0.9 V, evidencing the supercapacitor's continued stability. The CV profile, showing minor distortions, characterizes an electric double layer capacitor, linked to the microporosity and high functionality of COP. The COP superstructure creates a microporous charge transfer pathway beyond the side-by-side active sites for the ions, decreasing the diffusion resistance for ion storage and electrolyte infiltration. The FCF@PCOP-SO_3 electrode shows stable electrochemical behavior with good reversibility within the ΔV (V), extending up to 0.9 V. Fig. 7(E) shows a quantitative analysis of the influence of the potential window on C_{sp}. A sigmoidal-shape curve reveals the considerable increase of C_{sp} from 778.75 F g^{-1} to 1378.99 F g^{-1} as the ΔV was extended from 0.17 V to 0.89 V. The GCD measurements were performed in a two-electrode configuration to estimate the charge storage ability at different J values, ranging from 1–10 A g^{-1} over 0.0 to −0.87 V (Fig. 7(F)). The C_{sp} was evaluated with the following equation:[37]

$$C_{sp} = \frac{\Delta t I}{\Delta V m} \quad (3)$$

From the GCD curves, the C_{sp} of the FCF@PCOP-SO_3 electrode is found to be 670.79 F g^{-1} at the J value of 1 A g^{-1}. The approximately symmetric curve-like shapes of charge–discharge curves rather confirm the electric double layer capacitor energy storage mechanism. Even at the high J of 10 A g^{-1}, the discharge curves of FCF@PCOP-SO_3 exhibit only a partially low voltage drop (IR drop), showing low total resistance and excellent electrochemical reversibility. The impressive charge storage capabilities of the FCF@RCOP-SO_3 can be attributed to its porous structure, well-organized ion transport pathways, interconnected cavities, and superior wettability. The high hydrophilicity of the as-prepared COP is seen in the contact angle shown in Fig. 1(G) and the corresponding Supporting Videos VS1 and VS2 (ESI†). Moreover, the symmetry of the charge/discharge curves demonstrates the excellent capacitance characteristics of FCF@PCOP-SO_3.

Rate capability is an important factor in the selection of SCs for power applications. The SC capacity decreases slowly with the rise in current density, which is usually related to the ion diffusion resistance. Higher J values requires faster ion diffusion to make all the active materials available. The obstruction–diffusion effect limits the penetration of ions due to the time limitation, eventually resulting in some active surface areas being out of reach for charge storage. The relationship between energy density (ED, Wh kg^{-1}) and power density (PD, W kg^{-1}) was investigated to evaluate the overall performance of the energy storage source. The ED generally decreases with increasing PD. Fig. 7(G) displays the Ragone plot of FCF@PCOP-SO_3 at different J values (1 to 10 A g^{-1}) with the ΔV of 0.88 V. We calculated the PD and ED using the following equations:[37]

$$E_D = \frac{C_s}{2 \times 3.6}\Delta V^2 \quad (4)$$

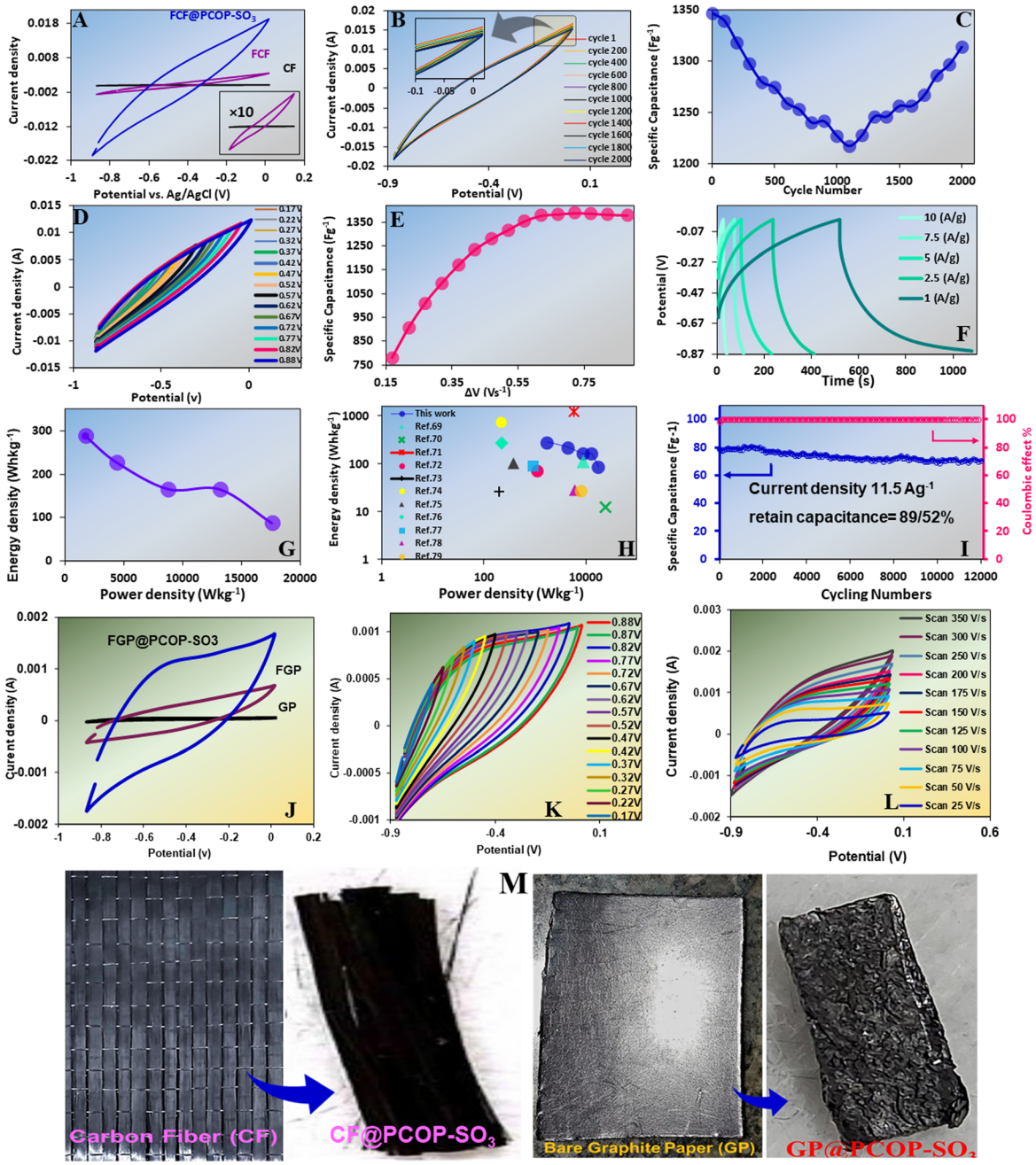

Fig. 7 Energy storage properties of FCF@PCOP-SO_3. (A) The comparative CVs. (B) Stability of shape and area for FCF@PCOP-SO_3 after 2000 successive CVs. (C) Calculated C_{sp} as a function of the cycle number for the FCF@PCOP-SO_3 electrode with a 2.44% loss of the initial value. (D) CVs as a function of potential, ranging from −0.87 to 0.01 V. (E) The calculated C_{sp} against the applied potential window. (F) GCD curves recorded at 1, 2.5, 5, 7.5 and 10 A g^{-1}. (G) The plot of ED *versus* PD. (H) Ragone plot related to ED and PD of the FCF@PCOP-SO_3 electrode compared with some recent values in literature.[40–50] (I) Long-term stability indexed with C_{sp} and coulombic efficiency after 12 000 cycles in 0.1 M H_2SO_4 aqueous electrolyte. (J) The comparative CVs in 0.1 M of H_2SO_4. (K) CVs as a function of potential window ranging from 0.17 to 0.88 V. (L) The effect of different sweeping rates on the shape of CVs from 25 to 350 mV s^{-1}. (M) Photographs taken of the CF and the FCF@PCOP-SO_3 (left) and GP and FGP@PCOP-SO_3 (right).

$$P_D = \frac{E \times 3600}{\Delta t} \quad (5)$$

The maximum ED of the FCF@PCOP-SO_3 is 288.59 Wh kg^{-1}, which decreased to 87.520 Wh kg^{-1} as the PD increased from 1760 to 17 600 W kg^{-1}. The large increase in ED may be due to the high V and the increase in capacitance due to faradaic reactions.[38] Further, the Ragone plot highlights the superior performance of FCF@PCOP-SO_3 toward other SCs in previous reports (Fig. 7(H)). The energy density of FCF@PCOP-SO_3 is comparable to or higher than that of most SCs. Another important parameter to be measured in the evaluation of the

changed electrode is the stability of the SC over repeated charge–discharge cycles. The symmetrical two-electrode configuration device with the FCF@PCOP-SO_3 electrode was subjected to a long-term cyclic stability test at a high J of 11.5 A g^{-1} with 89.52% retention of the initial C_{sp} after 12 000 cycles (Fig. 7(I)). Especially, the almost-symmetrical GCD curves showed a partial shape change with long-time cycling owing to: (i) an interconnected, predominantly porous structure for the rapid entry and extraction of ions, (ii) structural defects and active sites leading to high reactivity, and (iii) a functionalized porous framework with hopping mechanism for the transport of ions. In Fig. 7(I), the coulombic efficiency (CE) was obtained from the following equation:[39]

$$\mathrm{CE} = \frac{T_d}{T_c} \times 100, \quad (6)$$

where T_d is the charge time and T_c is the discharge time at the same current. The FCF@PCOP-SO_3 electrode shows nearly 100% retention after 12 000 cycles due to its good electrochemical stability and impressive charge/discharge reversibility, positioning itself as the perfect basis for the remarkable performance of the SC. Fig. 7(J)–(L) illustrate the CVs obtained from graphite paper bearing PCOP-SO_3 (labelled as GP@ PCOP-SO_3), highlighting the charge storage characteristics compared to those measured at the FCF. In addition, Fig. 7(M) shows photographs of both FCF- and GP-based PCOP-SO_3 electrodes and their corresponding bare counterpart.

Gerischer impedance: reflecting and absorbing boundary conditions

To gain more insight into the interfacial occurrence on the pore walls at the crystalline PCOP-SO_3, faradaic impedance spectroscopy studies were performed in acidic, neutral and alkaline media, a deeper investigation beyond the charge transfer properties to determine the degree of exchange reaction compared to the natural transport of the protonic species (H^+, H_2O and OH^-). As shown in Fig. 8(A), in H_2SO_4, the FCF shows a semicircle slightly deviated to a Warburg element (a diagonal line) in a small portion of the curve, indicating a semi-infinite transmission line model (TLM) in the high-frequency region. In an acidic medium, the protonated SO_3H groups acts as a semi-boundary reflecting surface. This behavior aligns closely with the limited case of finite-length Warburg (FLW) in the high-frequency region, which characterizes a surface with a blocking characteristic across a wide range of frequencies, leading to the observation of a semi-vertical line in the complex plane, a hallmark of an ideal capacitive response.[24] This finding is supported by the electrochemical data recorded in 0.1 M H_2SO_4 (see Fig. 7).

The TLM effectively defines the natural transport coupled with a chemical reaction occurring within the diffusion layer. From a physical perspective, the high-frequency TLM indicates a chemical–electrochemical–chemical (CEC) mechanism. The high-frequency Warburg portion is not affected by the particular type of boundary (reflective or adsorptive) at the end of the

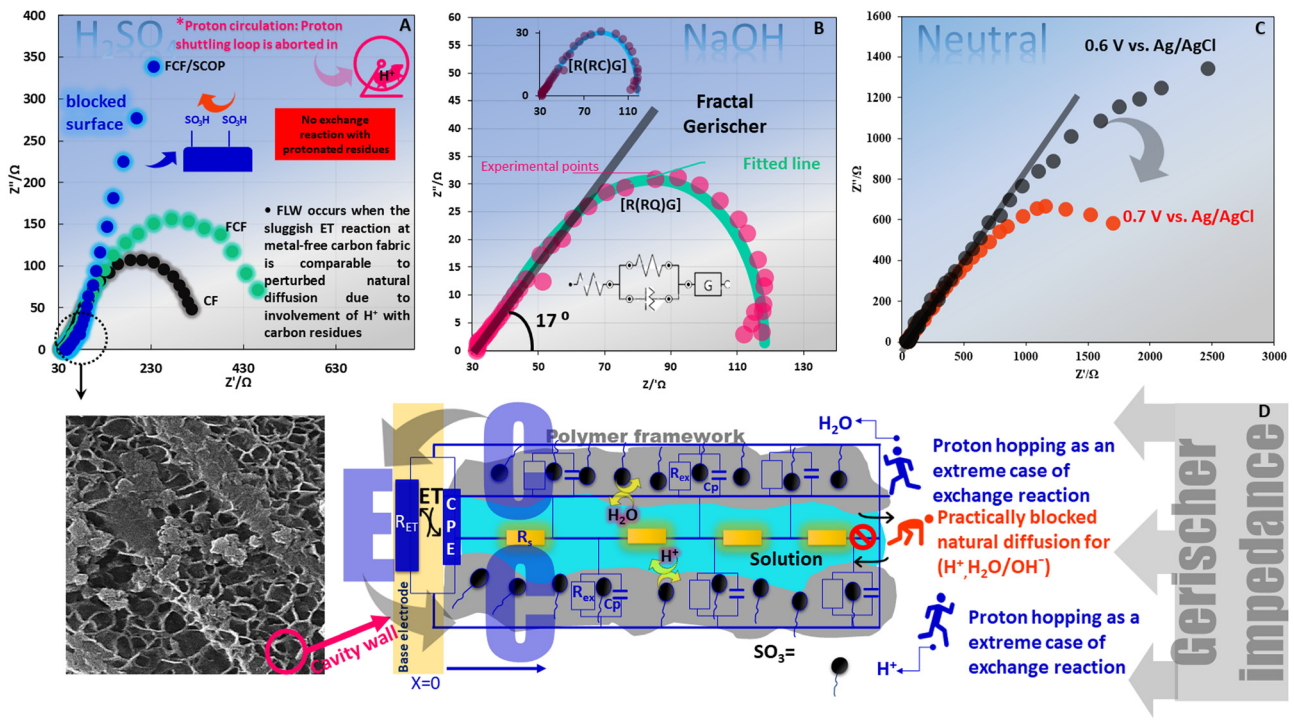

Fig. 8 The Nyquist plots are recorded in (A) 0.1 M H_2SO_4, (B) 0.1 NaOH, and (C) 0.1 M PBS (pH ≈ 7) at FCF@PCOP-SO_3. The inset of the middle plot displays the Gerischer element-included equivalent circuit. In an acidic environment, the protonated SO_3H effectively creates a blocking surface that aligns with the limited scenario of FLW, which describes a 'blocking' surface across most frequencies. This assumption leads to a semi-vertical line in the complex plane, signifying an ideal capacitor, a finding that is strongly reinforced by the data presented in Fig. 7. (D) A standard model for a CEC process defined by Gerischer impedance occurs during proton hopping within the walls of the PCOP.

diffusion zone. On this basis, there are also multiple features, namely, (i) the aborted chemical reaction, *i.e.*, a semi-reflective boundary condition; (ii) the rate of chemical reaction being lower than the natural transport ($R_s < R_{ex}$), so that the Nyquist plot in the high-frequency region shows a small Warburg part; and (iii) when the $R_s \gg R_{ex}$, the natural transport is practically blocked and proton hopping predominates the interfacial PCET reaction running at the applied DC potential. In Fig. 8(A), the blue curve is related to the FCF/PCOP interface where the protonation of the sulfonate groups in acidic medium blocks the possible exchange reaction when sweeping the frequency to the medium- and low-frequency regions (a semi-reflective boundary case, capacitive behavior), while the two non-sulfonated surfaces, CF and FCF, did not cause the behavior. In alkaline medium (Fig. 8(B)), the Nyquist plot displays a semicircle in the low-frequency region, although it continues through a 17° transmission line to the high frequencies instead of turning to the horizontal axis. The depressed transmission line instead of the conventional 45° beyond the perturbation of natural diffusion by exchange reaction reveals a fractal Gerischer (FG) impedance.[3,4] In systems with fractal geometry (*e.g.*, porous electrodes or rough surfaces), the diffusion process may demonstrate non-integer (fractal) dimensions, leading to a modified impedance response:[28]

$$\mathrm{ZFG}(\omega) = \frac{R}{[1 + [j\omega\tau]^{\alpha}]^{\beta}}, \quad (7)$$

where R is the resistance, ω is the angular frequency, τ is the characteristic time constant, j is the imaginary unit, and α, β are parameters related to the fractal dimension and the nature of the diffusion process. Based on the fact that the $-SO_3$ groups are also deprotonated in neutral medium (Fig. 8(C)), a similar Gerischer behavior emerges at 0.7 V *vs.* Ag/AgCl, although decreasing DC potential to 0.6 V apparently enlarges the charge transfer arc. The presence of the G element signifies an effective exchange reaction occurring between the functional groups located on the inner surfaces of crystalline channels.

In terms of Gerischer impedance, R_{ex} and R_s are represented by absolute values, referred to as the product values (R_G), which cannot be distinguished separately.[51] As schematically demonstrated in Fig. 8(D), the dominance of the exchange reaction over the inherent diffusion process is denoted as proton sinking.[3] This phenomenon suggests natural diffusion within a quasi-homogeneous medium is blocked by a hierarchical arrangement of functional groups. The time required for the exchange reaction involving sulfonate residues is less than that for their diffusion through COP cavities. The observed efficient exchange reaction between protonic species and internal residues in crystalline channels, combined with a KIE of less than 1.5, indicates a low potential barrier height for hydrogen bonds, which facilitates the proton transfer process. During the electrochemical step, the proposed active sites for the OER on non-metallic surfaces include heteroatom dopants (*e.g.*, –N, –S), polarized carbon atoms adjacent to polar groups, and surface defects, which facilitate the adsorption and activation of water molecules and reaction intermediates.[52–54] We hypothesize that OER proceeds *via* the adsorption of H_2O, OH, and OOH on nitrogen sites or polarized carbon atoms (*e.g.*, electron-deficient C–SO_3^-), forming surface hydrogen-bond networks (HBN) that promote the deprotonation of OH* to adjacent –SO_3^- groups.

Experimental evidence suggests that sulfonated porous covalent organic polymers (PCOP-SO_3^-) play three key roles in enhancing OER performance: (1) proton transport and PCET mechanism modification: the $-SO_3H$ groups facilitate efficient proton-coupled electron transfer (PCET) through hydrogen-bond networks. The observed kinetic isotope effect (KIE) values (<1.5, suggesting a secondary KIE) indicate that proton transfer is not involved in the rate-determining step (RDS), while pH-dependent studies confirm a non-concerted PCET mechanism. (2) Enhanced hydrophilicity: Improved wettability, as evidenced by contact angle measurements (Supporting Videos VS1 and VS2, ESI†), ensures better electrolyte accessibility to active sites. (3) Water cluster disruption: the –SO_3^- groups perturb bulk water clusters, increasing the availability of free water molecules and accelerating adsorption kinetics, as supported by attenuated total reflectance (ATR) spectroscopy (Fig. 6(D)).

4. Conclusions

This study presents a groundbreaking methodology for the synthesis of covalent organic polymers that exhibit a variety of distinct morphologies on carbon fabric surface. This approach not only broadens the scope of material design but also enhances our understanding of how structural variations can influence the properties and functionalities of these polymers toward heterogenous PCET reactions. A key finding of the study is the pivotal role that sulfonate groups play, giving a superior performance as a bifunctional metal-free PCET catalyst (proton relay) and supercapacitor. The presence of sulfonate groups significantly enhances the efficiency of OER in both basic and neutral media. This enhancement is attributed to the ability of sulfonate groups to stabilize charged intermediates. The intricate interfacial exchange reactions are facilitated by the sulfonated PCOP, which excelled beyond the concurrent activities occurring during electrocatalytic OER. This resulted in a pronounced extreme case of FLW manifesting in the high-frequency region of the Nyquist plot, identified as Gerischer impedance. This observation suggests that R_{exch} is significantly less than R_{diff}, indicating a proton-hopping mechanism. In summary, this research not only introduces a novel synthetic strategy for covalent organic polymers but also provides valuable insights into the relationship between polymer structure and reaction conditions, and it delivers mechanistic insights into the PCET mechanism on COP-type PCET catalysts.

Conflicts of interest

There are no conflicts to declare.

Data availability

The datasets used and/or analyzed in the current study are available from the corresponding author on reasonable request.

References

1 I. Popov, Z. Zhu, A. R. Young-Gonzales, R. L. Sacci, E. Mamontov, C. Gainaru, S. J. Paddison and A. P. Sokolov, *Commun. Chem.*, 2023, **6**, 77.
2 N. Sakashita, H. Ishikita and K. Saito, *Phys. Chem. Chem. Phys.*, 2020, **22**, 15831–15841.
3 R. Azizi, M. Shamsipur, A. Taherpour and A. Pashabadi, *J. Mater. Chem. A*, 2023, **11**, 1491–1502.
4 M. Shamsipur, M. Ardeshiri, A. A. Taherpour and A. Pashabadi, *J. Mater. Chem. A*, 2021, **9**, 2937–2947.
5 M. Shamsipur and A. Pashabadi, *Coord. Chem. Rev.*, 2019, **401**, 213068.
6 Q. Yang, H. Yu, Y. He, Z. Liu, C. Qin, B. Liu and Y. Li, *Eur. Polym. J.*, 2020, **123**, 109445.
7 K. Prakash, K. Chaudhary and D. T. Masram, *Appl. Catal., A*, 2020, **593**, 117411.
8 S. Hammes-Schiffer, *Chem. Rev.*, 2010, **110**, 6937–6938.
9 H. Ma, J. J. Chen, L. Tan, J. H. Bu, Y. Zhu, B. Tan and C. Zhang, *ACS Macro Lett.*, 2016, **5**, 1039–1043.
10 C. Zhang, Y. Liu, B. Li, B. Tan, C. F. Chen, H. B. Xu and X. L. Yang, *ACS Macro Lett.*, 2012, **1**, 190–193.
11 B. C. Patra, S. Khilari, R. N. Manna, S. Mondal, D. Pradhan, A. Pradhan and A. Bhaumik, *ACS Catal.*, 2017, **7**, 6120–6127.
12 Q. Liang, S. Cui, S. Xu, C. Yao, M. J. MacLachlan and Z. Li, *Chem. Commun.*, 2018, **54**, 3391–3394.
13 Q. Ma, R. Liao, Y. Lu, S. Liu, Y. Tang, Y. Zhu and D. Wu, *Chem. – Asian J.*, 2021, **16**, 3102–3106.
14 Z. Xiang, Y. Xue, D. Cao, L. Huang, J. F. Chen and L. Dai, *Angew. Chem., Int. Ed.*, 2014, **53**, 2433–2437.
15 A. Pradhan and R. N. Manna, *ACS Appl. Polym. Mater.*, 2021, **3**, 1376–1384.
16 Y. Li, P. Peng, F. Huo, X. Shao and Z. Xiang, *Front. Mater.*, 2019, **6**, 1–7.
17 D. D. Ma, C. Cao, X. Li, J. T. Cheng, L. L. Zhou, X. T. Wu and Q. L. Zhu, *Electrochim. Acta*, 2019, **321**, 134679.
18 Z. Liao, Y. Wang, Q. Wang, Y. Cheng and Z. Xiang, *Appl. Catal., B*, 2019, **243**, 204–211.
19 S. Gopi, K. Giribabu and M. Kathiresan, *ACS Omega*, 2018, **3**(6), 6251–6258, DOI: **10.1021/acsomega.8b00574**.
20 P. Peng, Z. Zhou, J. Guo and Z. Xiang, *ACS Energy Lett.*, 2017, **2**, 1308–1314.
21 H. Zhang, Z. Zhou, Y. Yin, H. Xu, Y. Wang, K. Yang, Z. Zhang, J. Wang and X. He, *EcoEnergy*, 2023, **1**, 217–247.
22 Z. Guo, S. Yang, M. Liu, Q. Xu and G. Zeng, *EcoEnergy*, 2024, **2**, 192–201.
23 M. Shamsipur and A. Pashabadi, *ChemElectroChem*, 2023, DOI: **10.1002/celc.202300423**.
24 J. Liu, J. Ren, Y. Du, X. Chen, M. Wang, Y. Liu and L. Wang, *Adv. Funct. Mater.*, 2024, **34**, 1–12.
25 X. Xie, J. Song, X. Fan, W. Zhao, K. Liu, Y. Zhao, L. B. Zhou, Y. Xiao, S. Li, H. Wang, G. Zhao, F. Xie, B. Song, Q. Guo, X. Jiao, P. He, F. Liu and Y. Zhang, *Adv. Funct. Mater.*, 2025, **2504467**, 1–9.
26 K. H. Ku, J. M. Shin, D. Klinger, S. G. Jang, R. C. Hayward, C. J. Hawker and B. J. Kim, *ACS Nano*, 2016, **10**, 5243–5251.
27 D. Ramimoghadam, M. Z. Bin Hussein and Y. H. Taufiq-Yap, *Int. J. Mol. Sci.*, 2012, **13**, 13275–13293.
28 A. Grimaud, O. Diaz-Morales, B. Han, W. T. Hong, Y. L. Lee, L. Giordano, K. A. Stoerzinger, M. T. M. Koper and Y. Shao-Horn, *Nat. Chem.*, 2017, **9**, 457–465.
29 H. Kim, J. Park, I. Park, K. Jin, S. E. Jerng, S. H. Kim, K. T. Nam and K. Kang, *Nat. Commun.*, 2015, **6**, 8253.
30 J. Jana, K. C. Bhamu, Y. T. Ngo, S. G. Kang, J. S. Chung and S. H. Hur, *Appl. Surf. Sci.*, 2021, **562**, 150253.
31 K. Ahanjan, M. Shamsipur, A. Taherpour and A. Pashabadi, *Electrochim. Acta*, 2022, **433**, 1–23.
32 S. Cotugno, D. Larobina, G. Mensitieri, P. Musto and G. Ragosta, *Polymer*, 2001, **42**, 6431–6438.
33 M. Thouvenin, I. Linossier, O. Sire, J. J. Péron and K. Vallée-Réhel, *Macromolecules*, 2002, **35**, 489–498.
34 M. Shamsipur, A. A. Taherpour and A. Pashabadi, *Ultrason. Sonochem.*, 2018, **42**, 381–389.
35 N. Vogel, *Spectroscopic Investigations of Hydrogen Bond Network Structures in Water Clusters*, 2013.
36 G. Ghanashyam and H. K. Jeong, *Chem. Phys. Lett.*, 2019, **722**, 39–43.
37 L. He, Y. Liu, C. Li, D. Yang, W. Wang, W. Yan, W. Zhou, Z. Wu, L. Wang, Q. Huang, Y. Zhu, Y. Chen, L. Fu, X. Hou and Y. Wu, *ACS Appl. Energy Mater.*, 2019, **2**, 5835–5842.
38 J. Yan, Z. Fan, W. Sun, G. Ning, T. Wei, Q. Zhang, R. Zhang, L. Zhi and F. Wei, *Adv. Funct. Mater.*, 2012, **22**, 2632–2641.
39 G. Ghanashyam and H. K. Jeong, *J. Energy Storage*, 2020, **30**, 101545.
40 M. Hu, H. Zhang and R. Lv, *Prog. Nat. Sci.: Mater. Int.*, 2020, **30**, 20–27.
41 G. Aruchamy and S. Thangavelu, *Electrochim. Acta*, 2020, **344**, 1–17.
42 P. Zhou, J. Weng, X. Liu, Y. Li, L. Wang, X. Wu, T. Zhou, J. Zhou and S. Zhuo, *J. Power Sources*, 2019, **414**, 210–217.
43 Z. Song, J. Wu, G. Li, X. Wang, T. Zhu, C. Geng, N. Liu, L. Fan and J. Lin, *J. Electroanal. Chem.*, 2020, **863**, 114040.
44 M. Vinayagam, R. Suresh Babu, A. Sivasamy and A. L. Ferreira de Barros, *Biomass Bioenergy*, 2020, **143**, 105838.
45 A. I. Mtz-Enriquez, A. I. Oliva, C. Gomez-Solis, J. Martinez-Ligas, M. Velazquez-Manzanares and J. Oliva, *Synth. Met.*, 2020, **261**, 116327.
46 H. Duan, T. Wang, X. Wu, Z. Su, J. Zhuang, S. Liu, R. Zhu, C. Changyun and H. Pang, *Chin. Chem. Lett.*, 2020, **31**(9), 2330–2332.
47 L. Han, H. Huang, X. Fu, J. Li, Z. Yang, X. Liu, L. Pan and M. Xu, *Chem. Eng. J.*, 2020, **392**, 1–7.
48 S. Zang, J. Jiang, Y. An, Z. Li, H. Guo, Y. Sun, H. Dou and X. Zhang, *J. Electroanal. Chem.*, 2020, **876**, 114723.

49 X. Wu, M. Yu, J. Liu, S. Li and X. Zhang, *J. Power Sources*, 2020, **464**, DOI: 10.1016/j.jpowsour.2020.228203.
50 S. Zhang, B. S. Huang, C. Shi, Q. Xu and Y. Zhu, *Colloids Surf., A*, 2020, **605**, 125243.
51 J. Bisquert, I. Mora-Sero and F. Fabregat-Santiago, *ChemElectroChem*, 2014, **1**, 289–296.
52 T. Xing, Y. Zheng, L. H. Li, C. C. Bruce, D. Cowie, S. Z. Gunzelmann, S. Qiao, Y. Huang and Y. Chen, *ACS Nano*, 2014, **8**, 6856–6862.
53 H. Li, H. Shang, Y. Shi, R. Yakimova, M. Syväjärvi, L. Zhang and J. Sun, *J. Mater. Chem. A*, 2018, **6**, 24358.
54 M. Li, L. Zhang, Q. Xu, J. Niu and Z. Xia, *J. Catal.*, 2014, **314**, 66–72.